

# Fast ion swapping for quantum information processing

H. Kaufmann,<sup>1</sup> T. Ruster,<sup>1</sup> C. T. Schmiegelow,<sup>1,\*</sup> M. A. Luda,<sup>1,†</sup> V. Kaushal,<sup>1</sup>  
J. Schulz,<sup>1</sup> D. von Lindenfels,<sup>1</sup> F. Schmidt-Kaler,<sup>1</sup> and U. G. Poschinger<sup>1,‡</sup>

<sup>1</sup>*Institut für Physik, Universität Mainz, Staudingerweg 7, 55128 Mainz, Germany*

We demonstrate a SWAP gate between laser-cooled ions in a segmented microtrap via fast physical swapping of the ion positions. This operation is used in conjunction with qubit initialization, manipulation and readout, and with other types of shuttling operations such as linear transport and crystal separation and merging. Combining these operations, we perform quantum process tomography of the SWAP gate, obtaining a mean process fidelity of 99.5(5)%. The swap operation is demonstrated with motional excitations below 0.05(1) quanta for all six collective modes of a two-ion crystal, for a process duration of 42  $\mu$ s. Extending these techniques to three ions, we reverse the order of a three-ion crystal and reconstruct the truth table for this operation, resulting in a mean process fidelity of 99.96(13)% in the logical basis.

The last decade has seen substantial progress towards scalable quantum computing with trapped ions. Gate fidelities reach fault-tolerance thresholds [1], and first steps towards realizing decoherence-free qubits have been demonstrated [2]. Moreover, microfabricated, segmented ion traps continue to mature as an experimental low-noise environment [3, 4] hosting multi-qubit systems [5, 6]. In the seminal proposal from Kielpinsky, Monroe and Wineland [7] for such *quantum CCD chip*, scalability is reached through ion shuttling operations, where trapped-ion qubits are moved between different trap sites through application of suitable voltage waveforms to the trap electrodes. Since the first demonstration of ion shuttling in segmented traps [8], the development of trap control hardware has progressed [9, 10]. This has recently led to demonstrations of fast ion shuttling at low final motional excitation [11, 12].

It is currently an open question if a trapped-ion quantum computer should be based on large processing units hosting thousands of qubits [13, 14] or on a modular architecture of medium-sized nodes with photonic interconnectivity [15]. With current technology, the possibilities for high-fidelity coherent control and readout of ion strings consisting of more than a few ions are limited, such that ion shuttling is required in either case. For universal quantum computation, two-qubit gates need to be performed between arbitrary pairs of ions, such that reordering ion strings becomes a necessary. Furthermore, if multiple ion species [16] are employed for sympathetic cooling [17] or ancilla-based syndrome readout via inter-species entangling gates [18, 19], deterministic ion reconfiguration is ultimately required.

To that end, segmented ion traps bearing junctions with T[20], X[21, 22] or Y[23] geometry have been developed and tested. Junctions increase the design complexity of the traps and allow only for sequential ion transport. Shuttling through junctions may yield large motional excitations, which precludes the execution of two-qubit gates. In this work, we perform ion reorder-

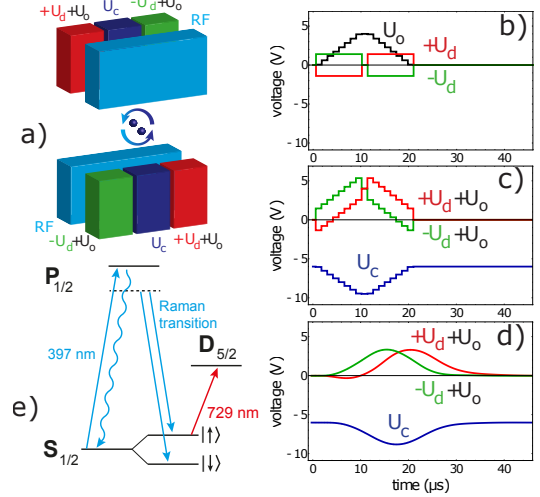


FIG. 1. Ion swapping in a multilayer segmented trap. **a)** shows the relevant trap electrodes, indicating where trapping voltage  $U_c$ , the diagonal voltage  $U_d$  and the offset voltage  $U_o$  controlling the process are applied. Panels **b)** and **c)** show the voltage ramps in the form of discrete samples, as they are programmed to the arbitrary waveform generator. Here **b)** shows  $U_d$  and  $U_o$ , while **c)** shows the actual electrode voltages. Panel **d)** shows the voltage ramps, measured after the external 50 kHz second-order low-pass filter, which leads to smoothing, but also to delay and increase of duration of the ramps. **e)** shows the relevant part of the level scheme of  $^{40}\text{Ca}^+$ .

ing via on-site swapping of ions through application of suitable electric potentials. The advantages of this operation are that it does not require sophisticated electrode structures, and that parallel multi-site swappings could be performed. While it has been shown [24] that segmented traps allow for deterministic ion swapping, we demonstrate this process on fast timescales, comparable to qubit operation times. Importantly, motional excitation is avoided, such that the ions stay within the Lamb-Dicke regime for all six collective modes of vibration of a two-ion crystal. To highlight that this operation is deterministic and that it can be used in conjunction with other qubit operations, we integrate it within a sequence

of shuttling, separation [12, 25, 26] and merging operations and qubit manipulations to realize a full quantum process tomography of the SWAP gate. By performing the swap operation on near-ground-state cooled ions and combining it with qubit manipulations and other shuttling operations, we demonstrate its potential use for scalable quantum logic with trapped ions.

For our experiments, we trap  $^{40}\text{Ca}^+$  ions in a segmented Paul trap similar to the design from [27]. Qubits are encoded in the Zeeman sublevels of the ground state  $|\downarrow\rangle \equiv |S_{1/2}, m_J = -\frac{1}{2}\rangle$  and  $|\uparrow\rangle \equiv |S_{1/2}, m_J = +\frac{1}{2}\rangle$ , where an external magnetic field lifts the degeneracy by  $2\pi \times 10.4$  MHz. The ions are laser cooled on the  $S_{1/2} \leftrightarrow P_{1/2}$  (cycling) dipole transition near 397 nm. Qubit initialization with a fidelity  $>99.8\%$  is achieved via optical pumping utilizing the narrow  $S_{1/2} \leftrightarrow D_{5/2}$  quadrupole transition near 729 nm [28]. For qubit manipulation, we employ stimulated Raman transitions mediated by a co-propagating pair of laser beams near 397 nm, detuned by  $2\pi \times 250$  GHz from the cycling transition. For sideband cooling and measurements of the motional state, we employ pairwise orthogonal propagating Raman beams, where the difference wavevector is aligned parallel (orthogonal) to the trap axis, providing coupling to axial (radial) modes of oscillation. Qubit readout is accomplished by spin-selective population transfer to the metastable  $D_{5/2}$  state, followed by detection of state-dependent resonance fluorescence with a photomultiplier tube [28]. All lasers are directed at the laser interaction zone (LIZ), see Fig. 3. As the Raman beams driving the single-qubit operations are co-propagating, and the laser near 729 nm for electron shelving is directed perpendicularly to the trap axis, both operations are insensitive to ion motion along the trap axis. Control of the ion motion is achieved by individual supply of the trap electrodes by a fast multichannel arbitrary waveform generator [11, 25] at analog update rates of up to 2.5 MSamples/s, where each signal line has a second-order II-type low-pass filter with a cutoff frequency of  $2\pi \times 50$  kHz.

The on-site swapping process of a two-ion crystal is depicted in Fig. 1. We start with the crystal axially confined via a trapping voltage  $U_c$  applied to the trapping electrode pair (blue segments in Fig. 1). Control over the rotation of the ion crystal is achieved via a diagonal, symmetry breaking dc quadrupole potential. This is generated by ramping up a voltage  $+(-)U_d$  to the electrodes neighboring the trap site, shown in green (red) in Fig. 1. Here, the polarity on the electrode pair left of the trapping site is inverted as compared to the polarity of the electrode pair to the right. With the diagonal potential applied, the trapping voltage  $U_c$  is gradually decreased, and a positive offset voltage  $U_o$  is ramped up at the neighboring segments. The corresponding increase of the axial confinement drives the ion crystal through a structural transition from horizontal to vertical alignment. Simultaneously, the

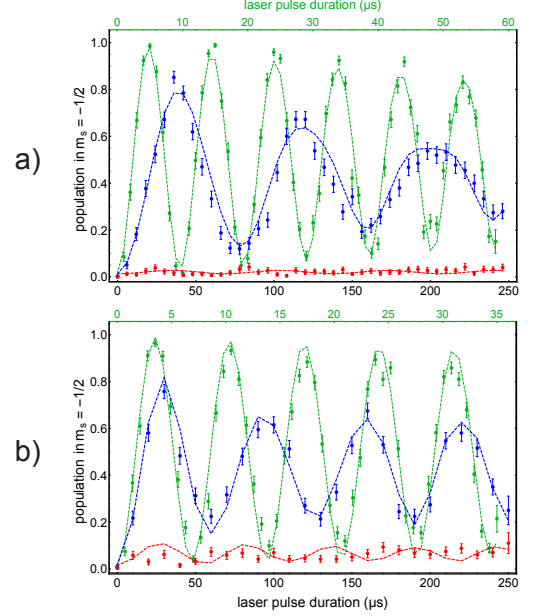


FIG. 2. Rabi oscillation data probed after swapping for verification of low-excitation swap operations: **a)** shows data for the axial center-of-mass mode, while **b)** shows data for the lower-frequency radial rocking mode. In both panels, the blue (red) points correspond to the blue (red) motional sideband, while the green points correspond to the carrier transition. The dashed lines are fits using model assuming oscillatory excitation. All curves indicate the probability for having at least one of the ions' state flipped to  $|\downarrow\rangle$ . Note that the time axis for the carrier data is scaled differently (upper axis ticks). Each data point corresponds to 200 state interrogations.

diagonal potential generated by  $U_d$  is ramped down to 0 V. With the ion crystal vertically aligned, the process is conducted in reverse order, with inverted polarity of the voltage  $U_d$  generating the diagonal potential.

We optimize the voltage ramps for the swap process by probing the final motional excitation on collective vibrational modes which are most affected, i.e. the axial *stretch* and the lower frequency radial *rocking* mode. The motional excitation is measured by driving Rabi oscillations on the red and blue motional sideband pertaining to all four radial and two axial collective modes of vibration. Each mode is cooled close to the ground state via resolved sideband cooling before the swapping operation, reaching mean phonon numbers between 0.016(4) (axial stretch mode) and 0.37(1) (lower frequency radial COM mode). Rabi oscillations are recorded over pulse areas in the range between  $6\pi$  and  $8\pi$  pertaining to the blue sideband Rabi frequency in the ground state. Fits assuming an oscillatory excitation, i.e. a coherent state of the corresponding mode, reveal the mean phonon number [11, 25, 29, 30].

Initially, a trapping voltage  $U_c = -6$  V yields horizontal crystal alignment at an axial center-of-mass (COM) vibrational frequency of  $2\pi \times 1.488$  MHz. The radial COM mode frequencies are  $2\pi \times 1.927$  MHz and

$2\pi \times 3.248$  MHz. We define the dimensionless time  $\tau = t/T$  for the total swapping time  $T$ . The least motional excitation is found for the following ramp parameters: The diagonal voltage  $U_d$  is ramped up rapidly within  $\tau=0.05$ , to an optimum value of 1.4 V. For driving the ion crystal into vertical alignment, the axial COM frequency has to exceed the lower radial COM frequency. To that end,  $U_c$  is ramped down to -9.5 V, while at the same time an additional offset voltage  $U_o = +4$  V is ramped up at all neighboring electrodes. Both  $U_c$  and  $U_o$  are ramped within  $\tau=0.05$  to  $\tau=0.45$ . The polarity change of the diagonal voltage  $U_d$  happens during  $\tau=0.45$  to  $\tau=0.55$ . The resulting voltage ramps are depicted in Fig. 1.

The swapping operation was tested for increasing times  $T$ , until we found the shortest time with negligible motional excitation of  $T=22 \mu\text{s}$ , which -including the filters- corresponds to an actual duration of  $42 \mu\text{s}$ . We measure the mean phonon number increase for all modes, comparing to the reference measurements directly after sideband cooling. For the axial modes, we find mean phonon number increases of 0.05(1) phonons on the COM mode and 0.013(6) phonons on the stretch mode. For the lower-frequency radial modes, corresponding to the plane in which the crystal rotates, we obtain 0.03(2) phonons on the COM mode and 0.04(2) phonons on the rocking mode. The higher-frequency radial mode, which is least affected from the swapping, features 0.02(1) phonons on the COM and 0.01(1) phonons on the rocking mode. Rabi oscillation data probed after swapping is shown in Fig. 2 for the axial COM and lower frequency radial rocking modes.

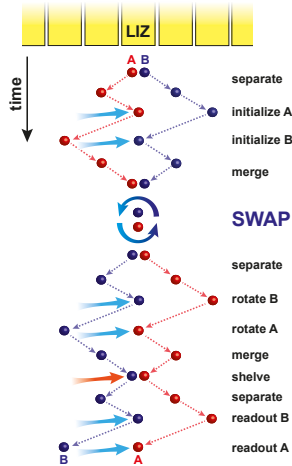


FIG. 3. Experimental quantum process tomography sequence for the SWAP operation. Each of the ion qubits A and B is shuttled to the laser interaction zone for initialization laser pulses, followed by a fast SWAP operation and subsequent individual qubit rotation laser pulses. Finally the state is read out via electron shelving and fluorescence detection.

Linear transport of ions along the trap axis is performed by gradually reducing the negative dc trapping voltage of  $U_c = -6$  V at the initial segment to 0 V, while applying a trapping voltage at the neighboring destination segment. We perform adiabatic transport at a duration of  $28 \mu\text{s}$  per trap segment pair, spaced by  $200 \mu\text{m}$ . Transport over more than one segment pair is performed by concatenation of this operation. Separation and merging operations require the transformation between single- and double-well potentials. The transient low axial confinement causes heating and oscillatory excitation [26]. We employ tailored voltage waveforms and proper cancellation of residual forces along the trap axis, enabling separation and merging of two-ion crystals within  $100 \mu\text{s}$  at a motional excitation of 5(2) quanta per ion [25].

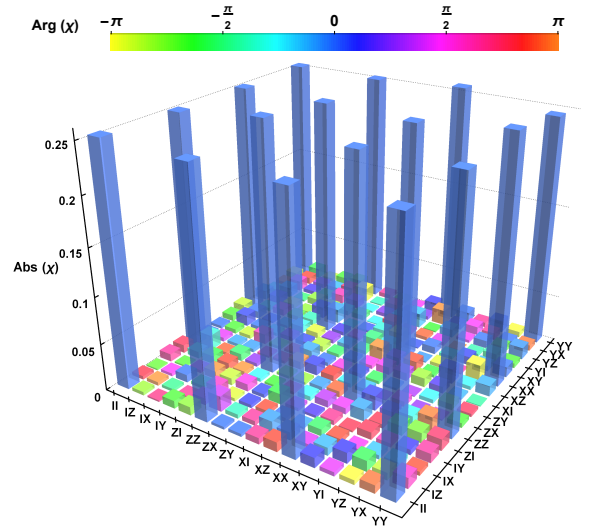


FIG. 4. Reconstructed process  $\chi$ -matrix for the SWAP operation. The absolute value of each matrix element is represented by the bar height, the phase is indicated by the color. The 16 elements which match the ideal absolute value of 0.25 have a controlled phase of  $\arg(\chi_{ij}) \approx 0$ . All other elements are close to the ideal value of zero and have random phases. Each of the 144 preparation/measurement settings is probed on average 1260 times.

The sequence for the process tomography consists of several shuttling operations and qubit manipulations, as depicted in Fig. 3. First, the two-ion crystal is prepared by Doppler cooling and pumping in the LIZ. After separation, each qubit is individually shuttled into the LIZ, where one of the operations  $\{\mathbb{I}, R_X(\pi/2), R_Y(\pi/2), R_X(\pi)\}$  is applied to bring the respective qubit to the state  $\{|\uparrow\rangle, |\uparrow\rangle - i|\downarrow\rangle, |\uparrow\rangle - |\downarrow\rangle, |\downarrow\rangle\}$ . The ions are recombined in the LIZ, where the swapping takes place. The crystal is again separated, and the ions are individually exposed to the analysis pulses  $\{\mathbb{I}, R_X(\pi/2), R_Y(\pi/2)\}$  for measuring the operators  $\{\sigma_z, \sigma_y, \sigma_x\}$ . After another merging operation in

the LIZ, the population transfer  $|\uparrow\rangle \leftrightarrow |D_{5/2}\rangle$  takes place. The ions are again separated and individually shuttled to the LIZ, where state dependent fluorescence is observed. Both qubits are shelved before fluorescence detection, to avoid depolarization of a remotely stored qubit from scattered light near 397 nm during the readout of the other qubit. The analysis laser pulses have to be corrected for phases accumulated from moving the ions in the inhomogeneous magnetic field along the trap axis. Starting with the preparation pulse, qubit  $i$  located at axial position  $x_i(t)$  at time  $t$  accumulates a phase which is determined by the deviation of the magnetic field from its value at the LIZ,  $\Delta B(x)$ , as

$$\phi_i = \frac{\mu_B g_J}{\hbar} \int_{t_i^{(i)}}^{t_i^{(a)}} \Delta B(x_i(t)) dt. \quad (1)$$

Here,  $t_i^{(i)}$  denotes the instant of the state preparation pulse for qubit  $i$  and  $t_i^{(a)}$  denotes the instant for its analysis pulse. The magnetic field inhomogeneity along the trap axis is mapped out by using a single ion as a probe: Initialized in a superposition state, it is shuttled to the destination site  $x$  and kept on hold for variable time  $t$ . After shuttling back to the LIZ, a refocusing  $\pi$ -pulse is applied, followed by another wait time of duration  $t$  with the ion placed at the LIZ. Finally, state tomography reveals the accumulated phase  $\phi(x, t) = \frac{\mu_B g_J}{\hbar} \Delta B(x) \cdot t + \phi_0$ , where  $\phi_0$  is a constant phase accumulated during the shuttling. By performing such measurements for different phase accumulation times  $t$  at different locations  $x$ , we map out the qubit frequency shift across segments 18-22 with a mean accuracy of about  $2\pi \times 1$  Hz. With the positions  $x_i(t)$  computed from the sequence data and simulated electrostatic trap potentials [31], the phases  $\phi_i$  can be also computed and used for correcting the phases of the analysis pulses. For each of the 16 prepared states, 9 measurements are performed. Each measurement is independently repeated 1000 times. For each prepared state, a resulting density matrix is obtained via linear inversion. From these density matrices, the process  $\chi$ -matrix is obtained via a second linear inversion. Computing the trace norm  $Tr(\chi_{meas}^\dagger \chi_{ideal})$ , we find a mean process fidelity of 98.1(5)%. We also perform process tomography without a SWAP operation, obtaining a mean process fidelity of 98.7(4)%. Thus, on the given level of accuracy, we conclude that the SWAP operation does not significantly affect the measured process fidelity, which is limited mainly by readout errors and systematic errors of the correction phases. Applying correction for readout errors, we obtain a mean process fidelity of 99.5(5)%. The resulting  $\chi$ -matrix is displayed in Fig. 4.

The techniques described above are extended to three qubits, where we demonstrate reordering from configuration  $ABC$  to configuration  $CBA$ . The detailed sequence can be found in the supplemental material [30]. Rather than performing quantum process tomography, we re-

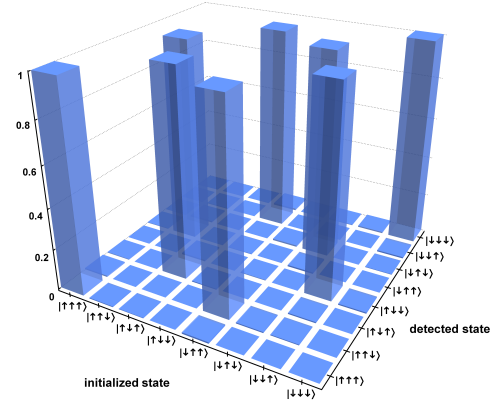


FIG. 5. Measured truth table of a three-ion crystal reconfiguration from  $ABC$  to  $CBA$  by using three consecutive two-ion SWAP operations. Each ion was initially prepared in either  $|\uparrow\rangle$  or  $|\downarrow\rangle$ , thus eight different input states are tested. Each input state is prepared and probed on average 2500 times. The measured probability to detect a particular state is represented by the height of the bars.

strict the measurements to the logical ( $Z$ ) basis, thus we reconstruct the logical truth table of the reordering operation. Starting from a three-ion crystal  $ABC$  in the LIZ, we separate into  $AB$  and  $C$  by performing the separation with a properly adjusted axial bias field. Ion  $C$  is moved to segment 26, then ions  $AB$  are moved back into the LIZ, where separation into  $A$  and  $B$  takes place. Then,  $A$ ,  $B$  and  $C$  are subsequently moved into the LIZ and initialized to either  $|\uparrow\rangle$  or  $|\downarrow\rangle$  by optical pumping. Now, the ions are merged pairwise at the LIZ, where swapping and subsequent separation take place. The respective third ion is stored six segments away to the left or right, such that its trapping potential does not affect the merging, swapping and separation operations. The three subsequent swappings  $AB \rightarrow BA$ ,  $AC \rightarrow CA$  and  $BC \rightarrow CB$  establish the desired order  $CBA$ . Then, the ions are individually moved to the LIZ for shelving, and then individually moved again to the LIZ for fluorescence readout. We measure the resulting spin configuration for eight different input states. The resulting truth table is shown in Fig. 5. We obtain a mean fidelity of 98.47(9)% in the logical basis. The mean fidelity with correction for readout errors is 99.96(13)%. The sequence consists of three separation, three merging, three swapping and 30 linear transport operations. The execution time of this process is 5.7 ms, where 93% of this time is devoted to shuttling operations.

In conclusion, we have demonstrated basic functionality of a quantum processing unit based on different shuttling operations, including qubit register reconfiguration. It is shown that operations such as initialization, coherent manipulation and readout are not affected by swapping and other shuttling operations. In future experiments, the time required for such shuttling operations will be substantially reduced by several measures:



Compensation of filter-induced waveform distortion will allow for faster ion motion. A novel waveform generator with a voltage range of  $\pm 40$  V will enable tighter radial trapping, which will enable swap operations at larger radial trap frequencies. Furthermore, control techniques [32, 33] may be applied to enable faster shuttling. The shuttling-based quantum information processor requires the execution of entangling gates, which among all operations exhibit the strongest sensitivity to motional excitation. Here, we will exploit the fact that shuttling along the trap axis mainly affects axial modes of vibration, and carry out the entangling gates mediated by radial modes.

The research is based upon work supported by the Office of the Director of National Intelligence (ODNI), Intelligence Advanced Research Projects Activity (IARPA), via the U.S. Army Research Office grants W911NF-10-1-0284 and W911NF-16-1-0070. The views and conclusions contained herein are those of the authors and should not be interpreted as necessarily representing the official policies or endorsements, either expressed or implied, of the ODNI, IARPA, or the U.S. Government. The U.S. Government is authorized to reproduce and distribute reprints for Governmental purposes notwithstanding any copyright annotation thereon. Any opinions, findings, and conclusions or recommendations expressed in this material are those of the author(s) and do not necessarily reflect the view of the U.S. Army Research Office.

---

\* Present address: LIAF - Laboratorio de Iones y Atomos Frios, Departamento de Fisica & Instituto de Fisica de Buenos Aires, 1428 Buenos Aires, Argentina

† Present address: DEILAP, CITEDEF & CONICET, J.B. de La Salle 4397, 1603 Villa Martelli, Buenos Aires, Argentina

‡ poschin@uni-mainz.de

- [1] C. J. Ballance, T. P. Harty, N. M. Linke, M. A. Sepiol, and D. M. Lucas, (2015), arXiv:1512.04600 [quant-ph].
- [2] D. Nigg, M. Müller, E. A. Martinez, P. Schindler, M. Hennrich, T. Monz, M. A. Martin-Delgado, and R. Blatt, *Science* **345**, 302 (2014).
- [3] D. A. Hite, Y. Colombe, A. C. Wilson, K. R. Brown, U. Warring, R. Jördens, J. D. Jost, K. S. McKay, D. P. Pappas, D. Leibfried, and D. J. Wineland, *Phys. Rev. Lett.* **109**, 103001 (2012).
- [4] N. Daniilidis, S. Gerber, G. Bolloten, M. Ramm, A. Ransford, E. Ulin-Avila, I. Talukdar, and H. Häffner, *Phys. Rev. B* **89**, 245435 (2014).
- [5] J. P. Home, D. Hanneke, J. D. Jost, J. M. Amini, D. Leibfried, and D. J. Wineland, *Science* **325**, 1227 (2009).
- [6] C. D. Herold, S. D. Fallek, J. T. Merrill, A. M. Meier, K. R. Brown, C. Volin, and J. M. Amini, (2015), arXiv:1509.05378 [quant-ph].
- [7] D. Kielpinski, C. Monroe, and D. J. Wineland, *Nature* **417**, 709 (2002).
- [8] M. A. Rowe, A. Ben-Kish, B. DeMarco, D. Leibfried, V. Meyer, J. Beall, J. Britton, J. Hughes, W. M. Itano, B. Jelenkovic, C. Langer, T. Rosenband, and D. J. Wineland, *Quantum Inf. and Comput.* **2**, 257 (2002).
- [9] R. Bowler, U. Warring, J. W. Britton, B. C. Sawyer, and J. Amini, *Rev. Sci. Instrum.* **84**, 033108 (2013).
- [10] M. T. Baig, M. Johanning, A. Wiese, S. Heidbrink, M. Ziolkowski, and C. Wunderlich, *Rev. Sci. Instrum.* **84**, 124701 (2013).
- [11] A. Walther, F. Ziesel, T. Ruster, S. T. Dawkins, K. Ott, M. Hettrich, K. Singer, F. Schmidt-Kaler, and U. G. Poschinger, *Phys. Rev. Lett.* **109**, 080501 (2012).
- [12] R. Bowler, J. Gaebler, Y. Lin, T. R. Tan, D. Hanneke, J. D. Jost, J. P. Home, D. Leibfried, and D. J. Wineland, *Phys. Rev. Lett.* **109**, 080502 (2012).
- [13] A. M. Steane, *Quant. Inf. Comp.* **7**, 171 (2007).
- [14] B. Lekitsch, S. Weidt, A. G. Fowler, K. Mølmer, S. J. Devitt, C. Wunderlich, and W. K. Hensinger, (2015), arXiv:1508.00420 [quant-ph].
- [15] C. Monroe, R. Raussendorf, A. Ruthven, K. R. Brown, P. Maunz, L.-M. Duan, and J. Kim, *Phys. Rev. A* **89**, 022317 (2014).
- [16] J. P. Home, in *Advances in Atomic, Molecular, and Optical Physics*, Advances In Atomic, Molecular, and Optical Physics, Vol. 62, edited by P. R. B. Ennio Arimondo and C. C. Lin (Academic Press, 2013) pp. 231 – 277.
- [17] D. Kielpinski, B. E. King, C. J. Myatt, C. A. Sackett, Q. A. Turchette, W. M. Itano, C. Monroe, D. J. Wineland, and W. H. Zurek, *Phys. Rev. A* **61**, 032310 (2000).
- [18] C. J. Ballance, V. M. Schäfer, J. P. Home, D. J. Szwer, S. C. Webster, D. T. C. Allcock, N. M. Linke, T. P. Harty, D. P. L. A. Craik, D. N. Stacey, A. M. Steane, and D. M. Lucas, *Nature* **528**, 384 (2015).
- [19] T. R. Tan, J. P. Gaebler, Y. Lin, Y. Wan, R. Bowler, D. Leibfried, and D. J. Wineland, *Nature* **528**, 380 (2015).
- [20] W. K. Hensinger, S. Olmschenk, D. Stick, D. Hucul, M. Yeo, M. Acton, L. Deslauriers, C. Monroe, and J. Rabchuk, *Applied Physics Letters* **88**, 034101 (2006).
- [21] R. B. Blakestad, C. Ospelkaus, A. P. VanDevender, J. M. Amini, J. Britton, D. Leibfried, and D. J. Wineland, *Phys. Rev. Lett.* **102**, 153002 (2009).
- [22] K. Wright, J. M. Amini, D. L. Faircloth, C. Volin, S. C. Doret, H. Hayden, C.-S. Pai, D. W. Landgren, D. Denison, T. Killian, R. E. Slusher, and A. W. Harter, *New Journal of Physics* **15**, 033004 (2013).
- [23] G. Shu, G. Vittorini, A. Buikema, C. S. Nichols, C. Volin, D. Stick, and K. R. Brown, *Phys. Rev. A* **89**, 062308 (2014).
- [24] F. Splatt, M. Harlander, M. Brownnutt, F. Zähringer, R. Blatt, and W. Hänsel, *New Journal of Physics* **11**, 103008 (2009).
- [25] T. Ruster, C. Warschburger, H. Kaufmann, C. T. Schmiegelow, A. Walther, M. Hettrich, A. Pfister, V. Kaushal, F. Schmidt-Kaler, and U. G. Poschinger, *Phys. Rev. A* **90**, 033410 (2014).
- [26] H. Kaufmann, T. Ruster, C. T. Schmiegelow, F. Schmidt-Kaler, and U. G. Poschinger, *New Journal of Physics* **16**, 073012 (2014).
- [27] S. Schulz, U. Poschinger, F. Ziesel, and F. Schmidt-Kaler, *New J. Phys.* **10**, 045007 (2008).
- [28] U. G. Poschinger, G. Huber, F. Ziesel, M. Deiss, M. Hettrich, S. A. Schulz, G. Poulsen, M. Drewsen, R. J. Hendricks, K. Singer, and F. Schmidt-Kaler, *J. Phys. B: At. Mol. Opt. Phys.* **42**, 154013 (2009).

- [29] D. Leibfried, R. Blatt, C. Monroe, and D. Wineland, *Rev. Mod. Phys.* **75**, 281 (2003).
- [30] See Supplemental Material at [URL will be inserted by publisher] for a detailed error discussion.
- [31] K. Singer, U. G. Poschinger, M. Murphy, P. A. Ivanov, F. Ziesel, T. Calarco, and F. Schmidt-Kaler, *Review of Modern Physics* **82**, 2609 (2010).
- [32] H. A. Furst, M. H. Goerz, U. G. Poschinger, M. Murphy, S. Montangero, T. Calarco, F. Schmidt-Kaler, K. Singer, and C. P. Koch, *New Journal of Physics* **16**, 075007 (2014).
- [33] M. Palmero, S. Martinez-Garaot, U. G. Poschinger, A. Ruschhaupt, and J. G. Muga, *New Journal of Physics* **17**, 093031 (2015).

## Fast ion swapping for quantum information processing: supplemental material

H. Kaufmann,<sup>1</sup> T. Ruster,<sup>1</sup> C. T. Schmiegelow,<sup>1,\*</sup> M. A. Luda,<sup>1,†</sup> V. Kaushal,<sup>1</sup>  
J. Schulz,<sup>1</sup> D. von Lindenfels,<sup>1</sup> F. Schmidt-Kaler,<sup>1</sup> and U. G. Poschinger<sup>1,‡</sup>

<sup>1</sup>*Institut für Physik, Universität Mainz, Staudingerweg 7, 55128 Mainz, Germany*

### CONTENTS

I. Motional state readout	1
II. Process tomography	2
III. Three-ion crystal reconfiguration	6

### I. MOTIONAL STATE READOUT

To investigate the motional excitation from the swapping operation, we cool each of the six secular modes of the two ion crystal close to the motional ground state via resolved sideband cooling on the stimulated Raman transition. We either perform the swapping operation or wait for the respective duration to obtain reference data. Subsequently, we drive Rabi oscillations on the stimulated Raman transition, either the carrier (phonon number change  $\Delta n = 0$ ), red ( $\Delta n = -1$ ) or blue ( $\Delta n = +1$ ) sideband transition of the particular secular

mode to be measured on both ions for a variable time  $t$ . The ions are jointly shelved to the metastable state for spin readout, then the ion crystal is separated, and state-dependent fluorescence is observed individually for each ion. We thus obtain single ion data for sideband Rabi oscillations of the secular modes of the two ion crystal. The data for all secular modes is shown in Fig. 1 and Fig. 2.

We jointly fit the measurement data for carrier and sidebands to a model describing Rabi oscillations of two homogeneously driven ions on arbitrary sideband transitions, valid also outside the Lamb-Dicke regime. We consider an initial number state characterized by the phonon number  $n$  on mode  $i$ , and a phonon number difference per spin flip  $\Delta n$ , where  $\Delta n = +(-)1$  for the first blue (red) sideband. The light-motion coupling for a given secular mode  $i$  is described by the carrier Rabi frequency  $\Omega$ , the Lamb-Dicke factor  $\eta_i$ , and the matrix elements

$$m_1 = M_{n,n+\Delta n} \quad (1)$$

$$m_2 = M_{n+\Delta n,n+2\Delta n},$$

where

$$M_{n,n'}(\eta_i) = \langle n' | e^{ik\hat{x}} | n \rangle = e^{-\eta_i^2/2} (\eta_i)^{|n'-n|} L_{n'<}^{|n'-n|}(\eta_i^2) \sqrt{\frac{n_{<}!}{n_{>}!}} \quad (2)$$

By analytically solving the time-dependent Schrödinger equation we obtain the following expressions for the prob-

abilities to find both ions in  $|\downarrow\rangle$ ,  $P_{\downarrow\downarrow}$ , both ions in  $|\uparrow\rangle$ ,  $P_{\uparrow\uparrow}$ , and both ions in different spin states,  $P_{\uparrow\downarrow} = P_{\downarrow\uparrow}$ :

$$\begin{aligned} P_{\uparrow\uparrow,\Delta n,\eta_i}(t) &= \left( \frac{1}{m_1^2 + m_2^2} \right)^2 \times \left[ m_2^4 + 2m_1^2 m_2^2 e^{-\gamma t} \cos \left( \sqrt{\frac{m_1^2 + m_2^2}{2}} \Omega t \right) + \frac{m_1^4}{2} \left( 1 + e^{-\gamma t} \cos \left( \sqrt{2(m_1^2 + m_2^2)} \Omega t \right) \right) \right] \\ P_{\downarrow\downarrow,\Delta n,\eta_i}(t) &= \left( \frac{m_1 m_2}{m_1^2 + m_2^2} \right)^2 \times \left[ \frac{3}{2} + \frac{1}{2} e^{-\gamma t} \cos \left( \sqrt{2(m_1^2 + m_2^2)} \Omega t \right) - 2e^{-\gamma t} \cos \left( \sqrt{\frac{m_1^2 + m_2^2}{2}} \Omega t \right) \right] \\ P_{\uparrow\downarrow,n,\Delta n,\eta_i}(t) &= P_{\downarrow\uparrow,n,\Delta n,\eta_i}(t) = \frac{m_1^2}{4(m_1^2 + m_2^2)} \left( 1 - e^{-\gamma t} \cos \left( \sqrt{2(m_1^2 + m_2^2)} \Omega t \right) \right) \end{aligned} \quad (3)$$

\* Present address: LIAF - Laboratorio de Iones y Atomos Frios, Departamento de Física & Instituto de Física de Buenos Aires, 1428 Buenos Aires, Argentina

† Present address: DEILAP, CITEDEF & CONICET, J.B. de La Salle 4397, 1603 Villa Martelli, Buenos Aires, Argentina

‡ poschin@uni-mainz.de

where  $n$  is the initial quantum number,  $\Delta n$  is the phonon number change per single spin flip, and  $t$  is the time of exposure to the driving field. We assume all secular modes of the ion crystal to be in a coherent (Glauber) state after the swapping operation. This assumption is justified as the duration of the swapping is small as compared to the inverse heating rates (typically 0.2 s per phonon on the axial COM mode), and the initial state is rather close to the ground state. Thermal and coherent excitation on spectator modes leads to dephasing of the Rabi oscillations, which is described empirically by the additional decay factors  $e^{-\gamma t}$ . For each spin configuration  $s_1 s_2$ , we describe the measured signals by averaging over  $P_{s_1 s_2, n, \Delta n, \eta_i}(t)$  and weighting with the phonon number distribution for a coherent state with mean phonon number  $\bar{n}_i$ :

$$P_{s_1 s_2, \bar{n}_i, \Delta n, \eta_i}(t) = \sum_{n=0}^N e^{-\bar{n}_i} \frac{\bar{n}_i^n}{n!} P_{s_1 s_2, n, \Delta n, \eta_i}(t), \quad (4)$$

where  $N$  is a cutoff phonon number. We use a fit to the first red and blue sidebands as well as the carrier transition to determine the average phonon number of each motional mode. For each fit, the floating parameters are  $\Omega, \eta_i$  and  $\bar{n}_i$ . The obtained phonon numbers are listed in table I.

As the fluorescence readout takes places separately for the two ions, the recorded signals correspond to the probability of finding ion 1 in  $|\downarrow\rangle$ ,  $P_{\downarrow\downarrow, \bar{n}_i, \Delta n, \eta_i}(t) + P_{\downarrow\uparrow, \bar{n}_i, \Delta n, \eta_i}(t)$  and of finding ion 2 in  $|\downarrow\rangle$ ,  $P_{\downarrow\downarrow, \bar{n}_i, \Delta n, \eta_i}(t) + P_{\uparrow\downarrow, \bar{n}_i, \Delta n, \eta_i}(t)$ . In the main manuscript, the average of these probabilities,  $\frac{1}{2}(P_{\downarrow\uparrow, \bar{n}_i, \Delta n, \eta_i}(t) + P_{\uparrow\downarrow, \bar{n}_i, \Delta n, \eta_i}(t) + 2P_{\downarrow\downarrow, \bar{n}_i, \Delta n, \eta_i}(t))$  is shown in Fig. 2.

motional mode	$\omega/2\pi$ (MHz)	$\eta$	$\bar{n}$	$\bar{n}$ increase
axial c.o.m.	1.488	0.127	0.082(6)	-
axial c.o.m. w/ SWAP	1.488	0.129	0.131(7)	0.049(9)
axial stretch	2.578	0.100	0.016(4)	-
axial stretch w/ SWAP	2.578	0.099	0.029(5)	0.013(6)
radial 1 c.o.m	1.927	0.069	0.365(13)	-
radial 1 c.o.m w/ SWAP	1.927	0.070	0.394(13)	0.029(18)
radial 1 rocking	1.195	0.090	0.14(10)	-
radial 1 rocking w/ SWAP	1.195	0.090	0.18(11)	0.041(15)
radial 2 c.o.m.	3.248	0.066	0.099(9)	-
radial 2 c.o.m. w/ SWAP	3.248	0.066	0.115(10)	0.015(14)
radial 2 rocking	2.875	0.072	0.069(8)	-
radial 2 rocking w/ SWAP	2.875	0.072	0.081(7)	0.012(10)

TABLE I. Measured phonon numbers on the six collective motional modes of a two ion crystal with and without the swapping operation. The column  $\bar{n}$  increase is the difference between a measurement with and without swapping and corresponds to the motional excitation from the swapping.

## II. PROCESS TOMOGRAPHY

For the measurements on full process tomography for two ions, 16 different settings for preparation  $s = \{s_1, s_2\}$  with  $s_i \in \{|\uparrow\rangle, |\uparrow\rangle - i|\downarrow\rangle, |\uparrow\rangle - |\downarrow\rangle, |\downarrow\rangle\}$  and 9 different setting for detection  $d = \{d_1, d_2\}$  with  $d_i \in \{Z, Y, X\}$  are probed. Each setting  $(s, d)$  is probed on average  $N$  times. Small fluctuations of the measurement numbers between different settings arise from postselection removal of events where ions are lost or crystal melting occurs, these fluctuations are ignored in the following. For each setting,  $N_f^{(s, d)}$  events out of  $N$  detections yield the fluorescence result  $f = \{f_1, f_2\}$ , where  $f_i \in \{\text{dark}, \text{bright}\}$ . From this data, event frequencies

$P_f^{(s, d)} = N_f^{(s, d)} / N$  are calculated. For a given preparation setting  $s$ , these frequencies are used for linear inversion to obtain the resulting density matrix  $\rho^{(s)}$ . The set of 16 resulting density matrices is used for a second linear inversion to obtain the resulting process matrix  $\chi_{meas}$ . The process fidelity  $F$  with respect to the ideal process  $\chi_{ideal}$  is then given by the trace norm  $F = \text{Tr}(\chi_{ideal}^\dagger \chi_{meas})$ .

We estimate confidence intervals for the mean process fidelity via parametric bootstrapping. For this, we generate 500 instances of random measurement data. For each instance, we use the event frequencies  $P_f^{(s, d)}$  to generate multivariate random integers  $\tilde{N}_f^{(s, d)}$ , drawn from a multinomial distribution  $f(\{\tilde{N}_f^{(s, d)}\}, \{P_f^{(s, d)}\})$ , where



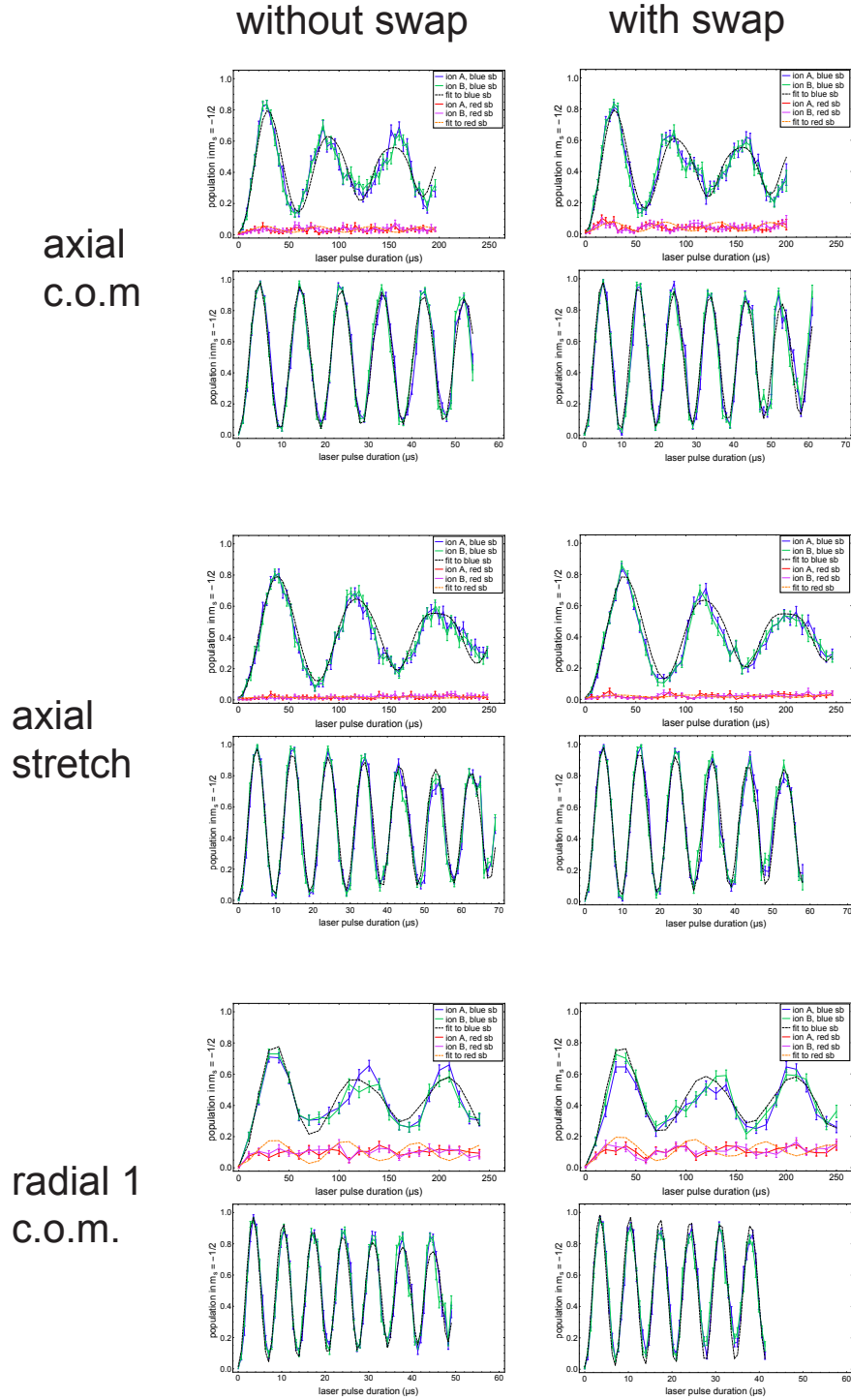


FIG. 1. Rabi oscillations on Raman transitions to investigate the motional excitation from the swapping operation. Left column: without the swapping operation but waiting for the corresponding amount of time after the initial cooling and before the analysis pulse. Right column: swapping operation after initial cooling. For each mode the carrier transition was measured additionally to the red and blue sideband. The blue color denotes ion A data and the green color denotes ion B data, as in the red sideband and blue sideband plots.

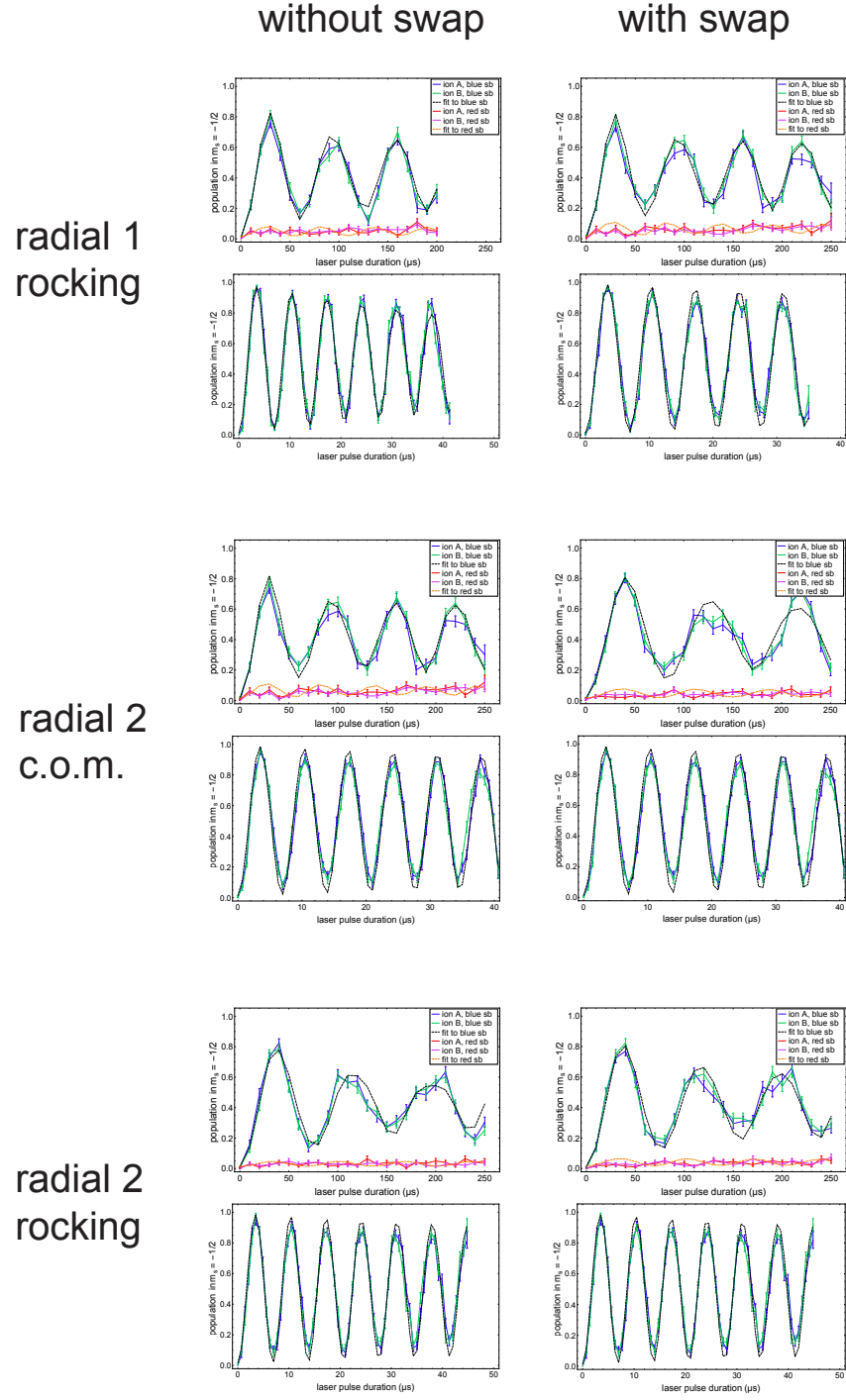


FIG. 2. Rabi oscillations on Raman transitions to investigate the motional excitation from the swapping operation. For each mode the carrier transition was measured additionally to the red and blue sideband. The blue color denotes ion A data and the green color denotes ion B data, as in the red sideband and blue sideband plots.

$\sum_f \tilde{N}_f^{(s,d)} = N$  and  $\sum_f P_f^{(s,d)} = 1$ . These random event numbers serve to calculate random event frequencies  $\tilde{P}_f^{(s,d)}$ , which are used in turn to generate random process matrices  $\tilde{\chi}_{meas}$ . Averaging over the 500 instances, we obtain the mean process fidelity along with a confidence interval.

In order to correct for readout errors, we perform the same procedure *without* SWAP operation, obtaining the event frequencies  $\tilde{P}_f^{(s,d)}$ , the density matrices  $\bar{\rho}^{(s)}$  and the process matrix  $\tilde{\chi}_{meas}$ . We restrict ourselves to the prepared spin configurations which are eigenstates of the  $Z_i$  operators,  $s' \in \{|\uparrow\uparrow\rangle, |\uparrow\downarrow\rangle, |\downarrow\uparrow\rangle, |\downarrow\downarrow\rangle\}$ . The diagonal elements of the reconstructed density matrices  $\bar{\rho}_{kk}^{(s')}$  indicate the conditional probabilities to detect fluorescence result  $f_k$  for preparation setting  $s'$  and detection setting  $d = Z_1 Z_2$ . Under the assumption of uncorrelated readout errors, these probabilities  $\bar{\rho}_{kk}^{(s')}$  are products of the probabilities to detect dark/bright events for the ion in  $|\uparrow\rangle/|\downarrow\rangle$  for each ion  $i$ :

$$\begin{aligned} \bar{\rho}_{kk}^{(s')} &= P_{f_k}^{(s', Z_1 Z_2)} \\ &= p_1(f_{k,1}|s'_1) \cdot p_2(f_{k,2}|s'_2), \end{aligned} \quad (5)$$

This holds under the assumption of perfect state preparation. It further holds that

$$\begin{aligned} p_i(\text{dark}_i | \uparrow_i) &\lesssim 1 \\ p_i(\text{bright}_i | \uparrow_i) &\gtrsim 0 \\ p_i(\text{dark}_i | \downarrow_i) &\gtrsim 0 \\ p_i(\text{bright}_i | \downarrow_i) &\lesssim 1 \\ p_i(\text{dark}_i | \uparrow_i) + p_i(\text{bright}_i | \uparrow_i) &= 1 \\ p_i(\text{dark}_i | \downarrow_i) + p_i(\text{bright}_i | \downarrow_i) &= 1 \end{aligned} \quad (6)$$

We calculate the readout probabilities  $p_i(f_{k,i}|s_i)$  by using the former normalization, e.g.

$$\begin{aligned} p_1(\text{dark}_1 | \uparrow_1) &= \frac{1}{2} P_{\text{dark}_1 \text{dark}_2}^{(\uparrow_1 \uparrow_2, Z_1 Z_2)} \\ &+ \frac{1}{2} P_{\text{dark}_1 \text{bright}_2}^{(\uparrow_1 \uparrow_2, Z_1 Z_2)} \\ &+ \frac{1}{2} P_{\text{dark}_1 \text{dark}_2}^{(\uparrow_1 \downarrow_2, Z_1 Z_2)} \\ &+ \frac{1}{2} P_{\text{dark}_1 \text{bright}_2}^{(\uparrow_1 \downarrow_2, Z_1 Z_2)} \end{aligned} \quad (7)$$

These readout probabilities are used to form the readout probability matrix  $M$ ,

$$M_{jk} = p_1(f_{j,1}|s'_{k,1}) \cdot p_2(f_{j,2}|s'_{k,2}). \quad (8)$$

This matrix determines the observed event frequencies *including* readout errors  $\tilde{P}_f^{(s,d)}$  from the event frequencies  $\hat{P}_f^{(s,d)}$  determined by the density matrix describing the state *before* readout:

$$\tilde{P}_f^{(s,d)} = M \cdot \hat{P}_f^{(s,d)}, \quad (9)$$

where the index  $f$  is running over the different observable fluorescence results. Thus, we can obtain the corrected event frequencies from

$$\hat{P}_f^{(s,d)} = M^{-1} \cdot \tilde{P}_f^{(s,d)}. \quad (10)$$

The corrected event frequencies can then be used for obtaining the process matrix as above, and parametric bootstrapping can be applied. From the fidelities obtained from parametric bootstrapping with the identity operation, we indeed obtain unit fidelity within the statistical error. This confirms the validity of the assumptions that the errors of preparation and single qubit rotations are insignificant as compared to readout errors, and that the readout errors are uncorrelated.

We can thus apply the readout error correction to the tomography data for the SWAP gate:

$$\hat{P}_f^{(s,d)} = M^{-1} \cdot P_f^{(s,d)}. \quad (11)$$

Performing parametric bootstrapping for this case, we also generate a random instance of the identity data along with the random instance of the SWAP data, such that both  $M^{-1}$  and  $\hat{P}_f^{(s,d)}$  are random quantities. This way, we take the statistical errors of the readout correction into account.

From the identity measurement, we infer the following readout probabilities:

$$\begin{aligned} p_1(\text{dark}_1 | \uparrow_1) &= 0.9941(7) \\ p_2(\text{dark}_2 | \uparrow_2) &= 0.9924(9) \\ p_1(\text{bright}_1 | \downarrow_1) &= 0.9888(10) \\ p_2(\text{bright}_2 | \downarrow_2) &= 0.9945(7) \end{aligned} \quad (12)$$

The resulting corrected process  $\chi$ -matrix is visualized in Fig. 4 of the main manuscript. Here, we additionally present the numerical data in Fig. 3:

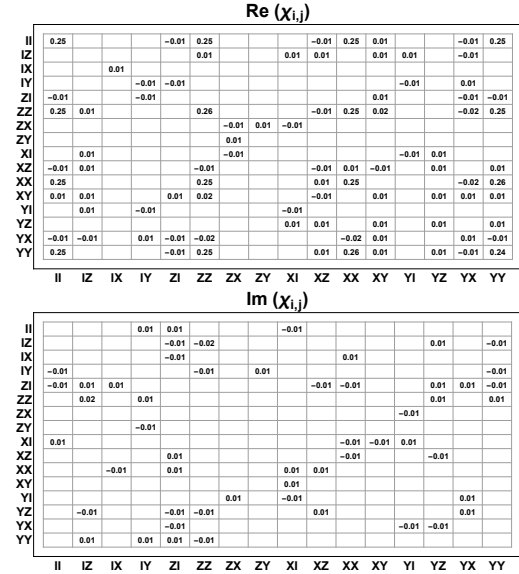


FIG. 3. Real and imaginary part of the  $\chi$ -matrix which was obtained in the quantum process tomography shown in Fig. 5 of the main manuscript. The absolute value of empty fields is smaller than 0.01.

For the three-ion measurements, we proceed in a similar way. There are however only 8 preparation settings, only one detection setting ( $Z$ ) and 8 fluorescence combinations. The observed event frequencies can be directly interpreted as elements of the process matrix in the truncated basis, such that no linear inversions are carried out and the readout correction can be directly applied. For the process fidelity in the truncated basis, we report the fidelities with significantly reduced statistical error, despite the fact that roughly the same number of measurements are used for each preparation setting. The reason for this is that we prepare *and* detect only in the logical basis in this case, which leads to detection event probabilities always close to either 0 or 1. This leads to reduced shot noise.

### III. THREE-ION CRYSTAL RECONFIGURATION

Here, we describe in detail how the reordering of the three-ion crystal  $ABC$  to  $CBA$  is accomplished. The experimental sequence is sketched in Fig. 4. The sequence starts with a three-ion crystal, trapped in a harmonic potential at electrode 20 which is called laser interaction zone (LIZ) since all lasers are targeted at this electrode. The sequence is partitioned in three sequences: *pre-sequence*, *main-sequence* and *post-sequence*. First, the pre-sequence is executed. Then, the main-sequence is executed and repeated 90 times. After the final repetition of the main sequence, the post-sequence is executed.

**Pre-sequence:** At the beginning of the pre-sequence, the three-ion crystal is Doppler cooled with a 397 nm laser. The crystal is then split by applying the separation voltage ramps with an additional calibrated axial bias field, such that the two ions  $A$  and  $B$  deterministically move to the left and ion  $C$  moves to the far right. The two-ion crystal  $AB$  is then shuttled to the LIZ, where Doppler cooling is applied. A potential well at electrode 14 is generated, which is of the same depth as on electrode 26, such that the potential well at the LIZ is properly centered and symmetric. The two-ion crystal  $AB$  is then separated, and each of the three ions  $A$ ,  $B$  and  $C$  is shuttled individually to the LIZ for Doppler cooling and detection of ion loss events. In this part of the sequence, only **sequential transports** are used, where one transport corresponds to the movement of one ion from one electrode to a neighboring electrode, while the other ions remain at their position.

**Main sequence:** In the main sequence, each ion is shuttled individually to the LIZ for Doppler cooling. Afterwards, each ion is optically pumped at the LIZ for state initialization to either  $|\uparrow\rangle$  or  $|\downarrow\rangle$ . The total state of the three ions is then initialized to one of eight possible configurations. Thus, the entire sequence is performed for each of the eight possible input states.

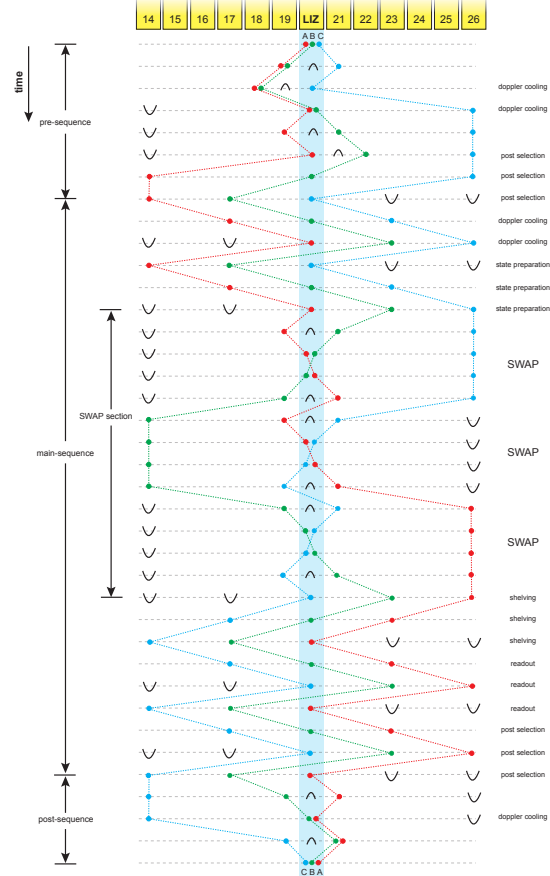


FIG. 4. Experimental sequence for the reconfiguration of a three ion crystal from  $ABC$  to  $CBA$  by using three consecutive two-ion SWAP operations. Black potential wells or barriers are applied to achieve a symmetric potential along the trap axis, thus placing the ions in the center of the laser beams.

Subsequently, the reordering of the three ions via two-ion swap operations is carried out. At first, the ions  $A$  and  $B$  are merged in the LIZ and the crystal swapping operation is executed. Thus, the order of the ions along the trap axis is changed to  $BAC$ . The two-ion crystal is then separated and the ions  $A$  and  $C$  are shuttled to the LIZ and merged together. Another swap operation is conducted, such that the order of the ions is changed to  $BCA$ . After that, the ions  $B$  and  $C$  are merged at the LIZ for a final swap operation to yield the desired order of  $CBA$ .

Afterwards, each ion is shuttled to the LIZ for electron shelving and subsequent detection of the spin state. It is important to perform the shelving operation on the ions *before* the detection operation takes place. The latter is done by illumination with 397 nm laser light, as residual stray light on an un-shelved ion can depolarize the

7

internal state, even if the ion is located several electrodes away.

In the main sequence, **parallel transports** are used, where all three separately trapped ions move simultaneously from one site to another. One parallel transport operation corresponds to the simultaneous movement of each of the ions from their initial electrode to one neighboring electrode.

**Post-sequence:** In the post-sequence, the individually trapped ions  $C, B$  and  $A$  are shuttled to the LIZ for post-selection of ion loss events. Afterwards, the ions  $A$  and  $B$  are merged, followed by a merging of the ion  $C$  to the two-ion crystal  $BA$ , thus yielding the three-ion crystal  $CBA$ .

The duration of the entire sequence amounts to 109.8 ms, while the most relevant part - the main sequence - takes 38.6 ms. The tables II -VI show more details on the shuttling operations which were employed. The shuttling operations require 23 % of the total duration of the main-sequence. In the following we explain the reason for this overhead and how to reduce it.

$ \uparrow\uparrow\uparrow\rangle$	1.001	0.007	0.003	0	0.002	0	0	0
$ \uparrow\uparrow\downarrow\rangle$	-0.004	0	0	0	0.998	0.006	0.003	0
$ \uparrow\downarrow\uparrow\rangle$	-0.002	0	1.002	0.007	0	0	0	0.001
$ \uparrow\downarrow\downarrow\rangle$	0	0	-0.004	0	-0.002	0	0.998	0.009
$ \downarrow\uparrow\uparrow\rangle$	-0.007	0.995	0	0.003	0	0.007	0	0
$ \downarrow\uparrow\downarrow\rangle$	0	-0.005	0	0	-0.007	1.001	0	0.003
$ \downarrow\downarrow\uparrow\rangle$	0	-0.004	-0.006	0.999	0	0	0	0.006
$ \downarrow\downarrow\downarrow\rangle$	0	0	0	-0.006	0	-0.002	-0.007	1.002

$|\uparrow\uparrow\uparrow\rangle \quad |\uparrow\uparrow\downarrow\rangle \quad |\uparrow\downarrow\uparrow\rangle \quad |\uparrow\downarrow\downarrow\rangle \quad |\downarrow\uparrow\uparrow\rangle \quad |\downarrow\uparrow\downarrow\rangle \quad |\downarrow\downarrow\uparrow\rangle \quad |\downarrow\downarrow\downarrow\rangle$

FIG. 5. Measured three ion truth table. Small negative values arise due to the readout error correction.

The swap operations require trap operation at a rather low RF level is required to make the swapping operation feasible, as the DC supply is limited to  $\pm 10$  V, and the axial confinement has to exceed the radial confinement in one direction during the swap operation. The low-frequency radial mode is only at  $\omega/2\pi = 1.93$  MHz. While we have verified that the excitation from the swapping operation is negligible, the linear transport operations add a slight amount of excitation if executed at low RF trap-drive amplitude. In the two-ion process tomography, this effect is negligible since only a few shuttling operations are used. By contrast, for the three-ion crystal reconfiguration, the amount of transport operations is way larger, such that we need to execute some of the shuttling operations more slowly for optimum readout fidelity.

In contrast to the two-ion measurements, the separation and merging operations are executed slower:  $260\mu\text{s}$  as compared to  $100\mu\text{s}$ . Also, the sequential transports

are slower:  $120\mu\text{s}$  as compared to  $28\mu\text{s}$ . This will be improved in future experiments, such that swapping can be executed at higher RF levels.

In Fig. 5, we show the data obtained for the three-ion measurements, which is also displayed as a bar chart in the main manuscript.

shuttling operation	duration ( $\mu$ s)	quantity
separation	260	2
sequential transport	120	31
total shuttling operation time	4.2 ms	
total sequence duration	39.7 ms	
percentage of shuttling operations	10.6 %	

TABLE II. Operations used in the **pre-sequence**.

operation	duration ( $\mu$ s)	quantity
separation	260	3
merging	260	3
sequential transport	120	30
parallel transport (3 ions)	100	48
SWAP	42	3
doppler cooling	2500	17
fluorescence detection	1200	6
shelving	600	3
other operations (spin init., dwell times, compensation pot. ramps)	1700	-
total shuttling operation time	10.1 ms	
total sequence duration	63.5 ms	
percentage of shuttling operations	15.9 %	

TABLE III. Shuttling operations used in the **main-sequence**.

operation	duration ( $\mu$ s)	quantity
separation	260	3
merging	260	3
sequential transport	120	30
SWAP	42	3
other operations (dwell times, compensation pot. ramps)	400	-
total shuttling operation time	5.3 ms	
total section duration	5.7 ms	

TABLE IV. Shuttling operations used in the **SWAP-section**.

shuttling operation	duration ( $\mu$ s)	quantity
merging	260	2
sequential transport	120	9
total shuttling operation time	1.6 ms	
total sequence duration	6.6 ms	
percentage of shuttling operations	24.3 %	

TABLE V. Shuttling operations used in the **post-sequence**.

shuttling operation	duration ( $\mu$ s)	quantity
separation	260	5
merging	260	5
sequential transport	120	70
parallel transport (3 ions)	100	48
SWAP	42	3
total shuttling operation time	15.9 ms	
total sequence duration	109.8 ms	
percentage of shuttling operations	14.5 %	

TABLE VI. Shuttling operations and timings used in the **entire sequence**.